

JET NOISE ABATEMENT VIA SURROGATE MODEL-BASED AEROACOUSTIC OPTIMISATION USING LARGE EDDY SIMULATION

Guangda Yang^{1,2,3}

¹Department of Aerospace Engineering, University of Bristol, Bristol, United Kingdom

²National Key Laboratory of Aircraft Configuration Design, Xi'an 710072, China

³Laboratory of Aerodynamic Noise Control, China Aerodynamic Research and Development Center, Mianyang, China

Abstract

Jet noise reduction has been the subject of both experimental and numerical studies for many years. In this paper, a surrogate model-based optimisation framework is presented which allows acoustic optimisation of jet nozzle exit geometries. The optimisation framework has been wrapped around an efficient LES solver, which is based on the CABARET scheme and is implemented on GPUs to make the run-times practical. The CABARET LES solutions are further coupled with the FW–H method for far-field noise predictions. The design space is modelled with nozzle chevron parameterisation, with the initial results presented here using chevron length and penetration angle as the design parameters. Effective geometric shape control and volume mesh deformation is achieved via an RBF volume interpolation approach with an efficient data reduction algorithm. Surrogate models are built for both thrust constraint and noise objective functions based on the OASPL values, and initial cases have been run using design-space investigation. The effectiveness, efficiency and robustness of the method is demonstrated, and initial results shown for cases with a thrust constraint. The significance of the thrust constraint and the objective function definition on the results is clearly shown via both single and multi-objective optimisations. There is a strong reduction of OASPL at low observation polar angles by increasing both the chevron length and penetration angle, with this dependence reversing at higher observer angles. Single point optimisations at any observation polar angle can achieve a decrease in OASPL.

Keywords: jet noise, aeroacoustic optimisation, surrogate model, large eddy simulation

1. Introduction

Aircraft noise has remained a problem over decades, and it is widely acknowledged as a limit to airline fleet growth and as a major concern for airport regulations. It is also acknowledged that aircraft noise can lead to detrimental effects on population health and thus incur enormous social cost in the long term. As a result, a considerable amount of research has been directed by major aviation industries, and also conducted in academia, towards better understanding of the noise generation mechanisms and development of tailored flow and noise control methods.

Engine noise is recognised as one of the major components of aircraft noise. The problem of noise generated from high-speed jets has been the focus of industrial and academic efforts for many years, and the technological advances in the design of the jet engines over the past decades have led to significant reduction of jet mixing noise. One typical example is to increase the bypass ratio of jet engines, which reduces noise due to a relatively lower exhaust flow velocity. Further reduction of jet mixing noise can be achieved by modifications of the nozzle geometry that can result in the use of non-axisymmetric nozzles and therefore very complex three-dimensional flows. For instance, it has been verified both experimentally [1, 2, 3] and computationally [4] that the use of chevron nozzles and non-concentric dual-stream nozzles can lead to jet mixing noise reduction.

With the maturity of computational fluid dynamics (CFD) and rapid development of computing power over the past decades, it enables the application of mainstream CFD in numerical optimal design,

which couples optimisation methods to numerical analysis tools to improve on a design objective. With respect to acoustic optimisation, it is desirable to employ high-fidelity flow analysis tools in order to capture the relevant flow physics to sufficient accuracy to be able to predict the aerodynamic results and acoustic signature accurately. However, the fact limitation on time budget and computational resources that is typical in engineering design cases makes it prohibitive for us to use high-fidelity flow solvers due to their computational expense. Previous work [5, 6] in the research community tend to use Reynolds-averaged Navier–Stokes (RANS) solver for jet nozzle acoustic optimisation. Nonetheless, it is still extremely expensive to perform nozzle acoustic optimisation effectively based on conventional RANS solvers using hundreds of CPUs [6], not to mention employing large-eddy simulation (LES) flow-solvers in practical design optimisation.

In recent years, new development in LES methods, such as the CABARET scheme [7, 8, 9], and its implementation on graphics processing units (GPUs) [10, 11, 12], has made it feasible to perform jet nozzle shape optimisations based on high-fidelity LES flow solvers. The aim of this work is to demonstrate a viable approach for acoustic optimisation of nozzle geometries using LES-based methods. In this work the objective is to mitigate the far-field noise signature by manipulation of the jet hydrodynamic field via nozzle shape optimisation. As such, a universal aerodynamic optimisation framework is developed that wraps around a high-fidelity LES flow solver. The optimisation design tools are then harnessed and applied to nozzle exit shape optimisation. In this paper, a representative isolated jet nozzle is chosen as the design case to demonstrate the effectiveness and efficiency of the optimisation framework.

2. Aerodynamic Optimisation Framework

This section primarily describes the components within the shape optimisation framework used herein, specifically the numerical methods for flow and aeroacoustic solutions, geometric shape control and surface and volume deformation algorithm, and the optimisation approach. The nozzle geometries considered in the current study are also briefly introduced in this section.

2.1 Computational Aeroacoustics

In this research, the jet flow and noise simulations are performed using the CABARET LES solver [7, 8, 9, 10, 11, 12], which is able to capture a wide variety of temporal scales typical of high-Reynolds-number flows. This Navier—Stokes solver is based on the low-dissipative and low-dispersive CABARET scheme, which is implemented with a wall model [13] and a synthetic turbulence boundary condition [14]. Thanks to its computational stencil simplicity and compactness, the CABARET method is implemented on unstructured hexagonal-dominant meshes of hanging-node type. In addition, an explicit asynchronous time-stepping scheme [15], which uses a hierarchy of local time steps depending on the local cell size, is used to march the flow solution at an optimal Courant—Friedrichs—Lewy (CFL) number. Compared to the single- or dual-time stepping, asynchronous time stepping can achieve a significant speed-up for computations with non-uniform meshes that are typically used for viscous flow simulations. Moreover, the CABARET implementation is performed with a small memory foot-print, which makes the LES solver feasible for running on GPUs, thereby further accelerating the computational speed and shortening the turnaround time. The GPU implementation together with asynchronous time-stepping approach makes the CABARET-LES of jet flow modelling possible in a reasonable time-frame and thus suitable for shape optimisation studies.

For the far-field noise calculations, the flow solver is coupled with the penetrable Ffowcs Williams—Hawkings (FW–H) integral surface method. In the FW–H method, the LES solution is recorded on a set of integration surfaces, which confine the jet turbulence and main vorticity regions in the jet shear layers, and then integrated with the analytical free-space Green's function solution to project the LES solution to the far-field sound.

2.2 Jet Nozzle Geometries of Consideration

In this study, a particular type of jet nozzle (i.e., chevron nozzles) in isolated configuration is considered as the design case to run numerical simulation and perform acoustic optimisation. A standard conical nozzle [2] (i.e., NASA SMC000) is selected as a baseline geometry, and different variants of the SMC nozzle are then chosen based on the results available in literature and those provided by

the industrial and advisory board partners. Figure 1 shows the schematic of several representative SMC-type chevron nozzles together with the round convergent SMC000 nozzle. It is worth noting that the SMC006 nozzle is used for investigation in this work. The setup for the optimisation case and its flow conditions are detailed in Section 3.1

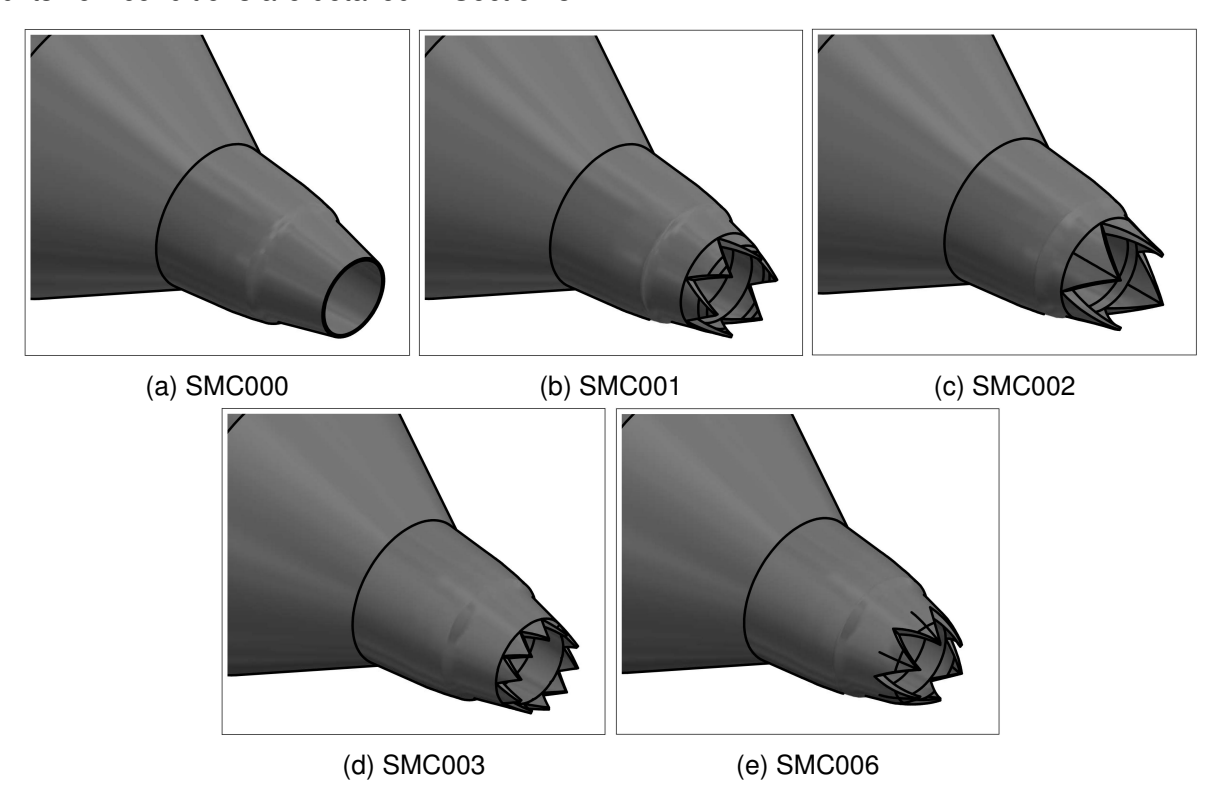


Figure 1 – Schematic of the various SMC-type nozzle configurations used in the present study.

2.3 Geometric Control and Mesh Deformation

Due to the nature of chevron nozzle geometries, key design parameters, such as penetration angle and chevron length, will be used to effectively explore the design space. In this work, radial basis function (RBF) interpolation is chosen as the method to control the design surface and also to deform the volume mesh. The RBF method has been extensively used in the authors' group in several areas, including fluid-structure coupling [16], optimisation [17], and adaptive sampling [18], owing to a number of desirable qualities. The RBF method can demonstrate robustness and the ability to preserve mesh quality for cases with large perturbations. The RBF method also allows global volume mesh interpolation throughout an n-dimensional space, which is solely based on the spatial coordinates of discrete base points (usually the deformed surface points). Hence, no connectivity information is required among the mesh points, thus making the RBF approach applicable to any mesh type. Nonetheless, a system matrix of the size of the number of control points needs to be solved, and this can become expensive for detailed surface meshes. Recent efforts have been made towards improving the effectiveness and efficiency of the RBF approach [19, 20, 21] with regard to mesh deformation using data reduction algorithms. Considering that large meshes are used in this study, it is essential to define a reduced set of control points for surface and volume mesh movement. There are many choices for the RBF to be used. In the current study, the popular Wendland's C2 function [22] is used due to its elegant compact support property, which means that it automatically ensures a strictly symmetric positive definite basis function matrix. In addition, the support radius of the basis function is appropriately chosen to avoid an ill-conditioned matrix for a very large-scale problem.

2.4 Optimisation Methodology

The goal of this research is to reduce the far-field noise signature by manipulating chevron nozzle parameters. Due to the cost of the objective evaluation from running LES, an adaptive sampling

surrogate model-based optimisation scheme has been developed. The RBF interpolation method is used to build an initial surrogate model. Since the dimension of the design space is low, for the initial design of experiment (DoE) the sampling points are evenly distributed in the design variable space. The evenly-spaced points sampling approach will also keep the RBF interpolation well conditioned. Once the objective variation is collected, the surrogate model is built and interrogated to identify promising regions of the design variable space from the initial budget of flow-solver calls. An adaptive sampling method is then employed for space-filling and search for the optimal value in the design space. Note that this has not been implemented in the initial design space studied here.

3. Optimisation Case Description

This section introduces the optimisation test case that is investigated in this work. Specifically, the jet nozzle selected for optimisation as well as its flow conditions are described herein. The validation of the CABARET-LES solver is provided for the physical properties from both aerodynamic and acoustic aspects. With respect to optimisation, two design variables are chosen and used to perturb the baseline nozzle geometry. The thrust is calculated and used as the design constraint to measure the nozzle performance. The spectral properties of far-field jet noise at multiple receiver locations are treated as the design objective.

3.1 Case Setup & Flow Conditions

The jet nozzle considered for optimisation in the present work is the SMC006 chevron nozzle as tested experimentally by Bridges and Brown [2] and also reported by Engblom *et al.* [23]. The SMC006 nozzle is serrated equally in the circumferential direction with six chevron tips and six notches with each chevron corresponding to a $\pi/3$ sector.

The mesh generation is accomplished by using the snappyHexMesh (sHM) utility within the open-source CFD package OpenFOAM. sHM can generate hexagonal-dominant meshes automatically from triangulated surface geometries (e.g., in STL format). The sHM utility also has the ability to generate layers of body-fitted grid near the boundaries. Figure 2 shows the sHM mesh of the SMC006 nozzle on the symmetry plane of the domain. The mesh was generated semi-automatically, and refinement is placed in regions near the nozzle exit to ensure the flow physics in the jet shear layer can be accurately captured. The presented mesh contains around 38 million cells. The SMC006 nozzle is placed in a position so that planes z=0 and y=0 cut right through a pair of tips and notches, respectively. Compared with the round SMC000 nozzle which has a 2-inch (i.e. $D_j=50.8\,\text{mm}$) exit diameter, SMC006 has a slightly reduced effective nozzle diameter due to the inward bending of the chevrons. It should be noted, however, that the diameter of SMC000 nozzle is used as the reference value in the present work for the purpose of consistency.

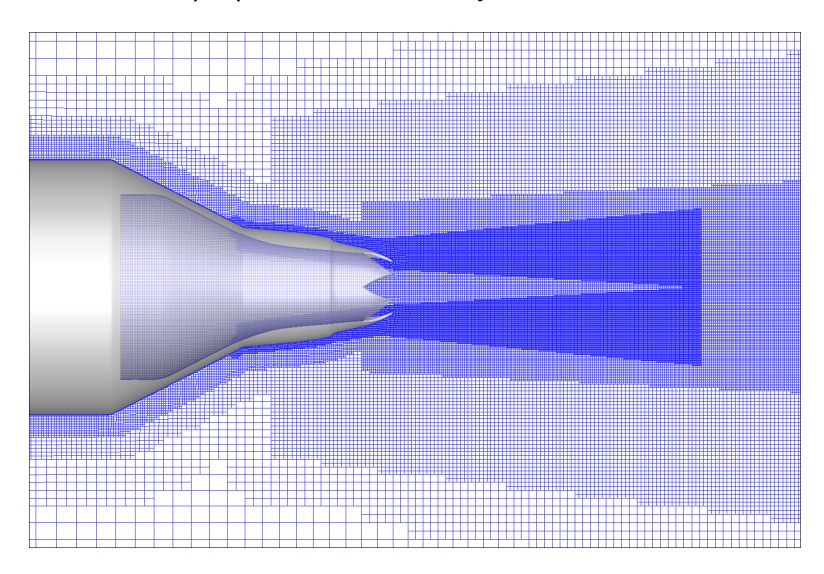


Figure 2 – Unstructured LES mesh (sHM) of isolated SMC006 nozzle at a cross section of the symmetry plane.

Special attention needs to be paid to construct a suitable FW–H surface. The acoustic integration surfaces typically include a conical surface and multiple closing discs. An example of the FW–H surfaces for the jet of the SMC006 nozzle is given in Fig. 3.

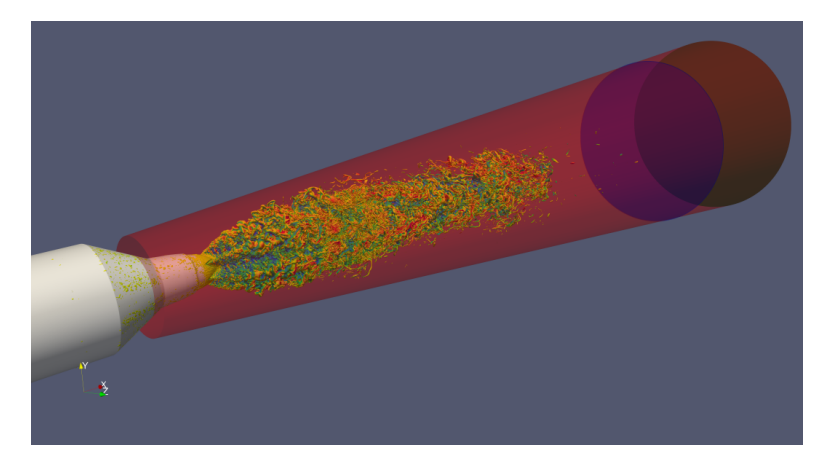
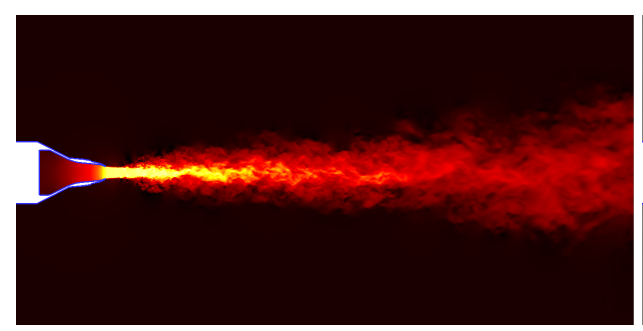
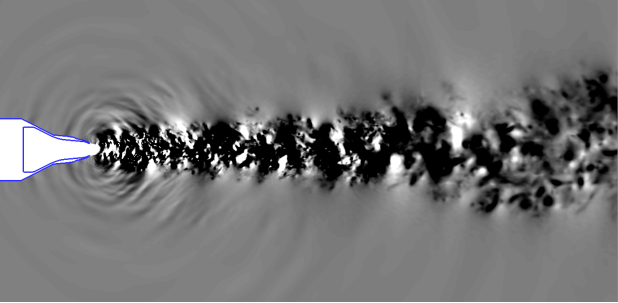


Figure 3 – Acoustic integration surfaces wrapping around the vorticity regions of the flow-field of the isolated SMC006 jet nozzle configuration.

The cold jet flow conditions correspond to set point (SP) 7 defined by Tanna [24], with an acoustic Mach number at the jet exit M=0.9 and a temperature ratio $T_j/T_\infty=0.84$. The ambient conditions are $p_\infty=101325\,\mathrm{Pa}$ and $T_\infty=288.15\,\mathrm{K}$. The total pressure and total temperature are imposed at the nozzle inlet such that the required jet stream velocity U_j is generated at nozzle exit. Some instantaneous flow-field results on the symmetry plane are presented in Fig. 4 for the SMC006 nozzle.





(a) Axial velocity magnitude (m/s) <0,340>

(b) Pressure amplitude, $P - P_{\infty}$ (Pa) <-500,500>

Figure 4 – Instantaneous jet flow-field of the CABARET-LES solution of SMC006 nozzle at SP 7 (M = 0.9).

3.2 Flow-Solver Validation

The CABARET LES calculations have been performed on a HPC cluster equipped with Nvidia Tesla P100 (16GB) GPU cards. The first 200 TUs (Time Units, 1 TU = D_j/U_j) are used as the transient time to reach a statistically stationary LES solution, and the collection time for the subsequent statistical analysis corresponds to a further 400 TUs. Hence, the total time for the solution of CABARET LES is 600 TUs.

The mean axial velocity on the centerline of the jet is compared in Fig. 5 between the CABARET-LES solution and experimental data, and a good agreement is observed. As shown in Fig. 6, the flow-field results at various positions downstream of the nozzle exit are also compared with the particle image velocimetry (PIV) data. The LES results compare very well with the experimental data.

With respect to the acoustic signature, Figure 7 shows the sketch of the positions of the far-field sound observers. The FW–H power spectral density (PSD) of the far-field sound at two representative polar angles are shown and compared with experimental data [26] in Fig. 8. The CABARET-LES results agree well with the experimental data, and the highest frequency where the physics are well captured

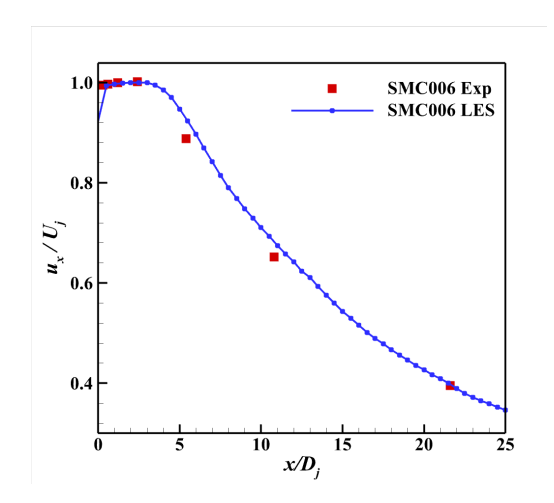


Figure 5 – Jet centerline profile of axial mean flow velocity component, compared to the consensus PIV data [2].

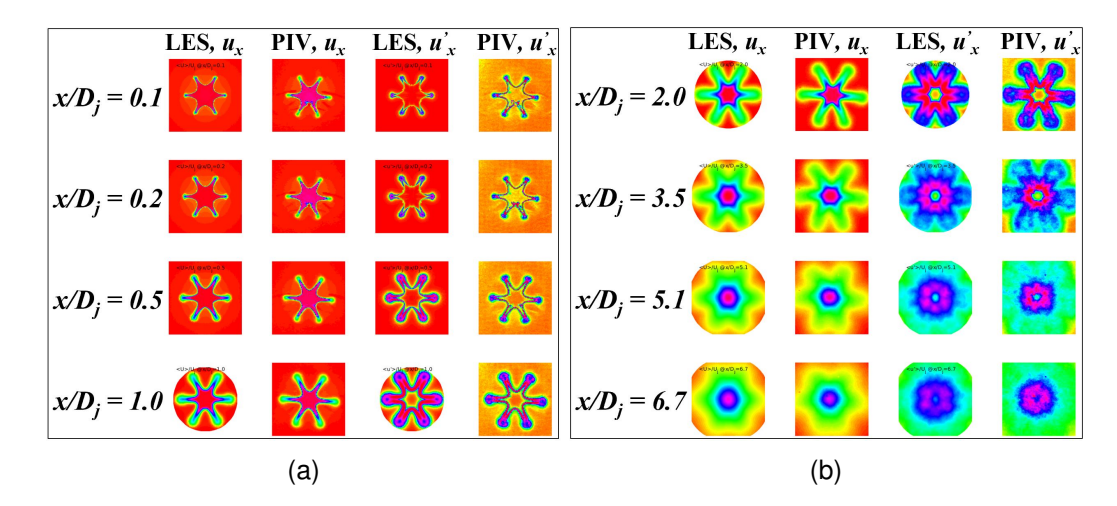


Figure 6 – Jet flow-field for SMC006 nozzle at different streamwise locations, comparison between CABARET-LES results and NASA PIV data.

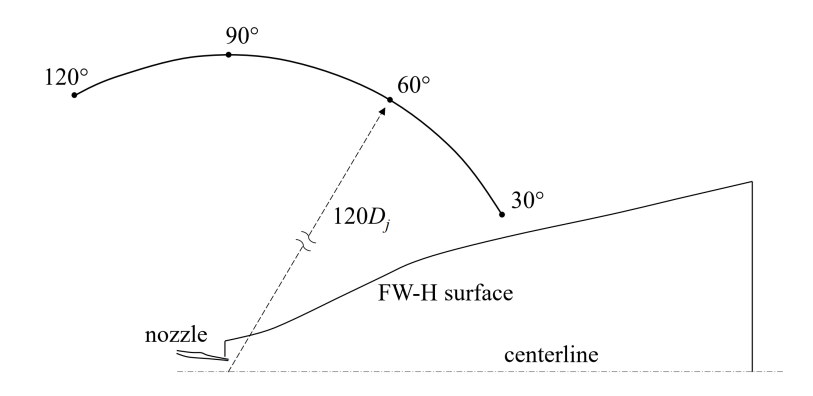


Figure 7 – Schematic of the far-field sound observer positions. (Reference [25])

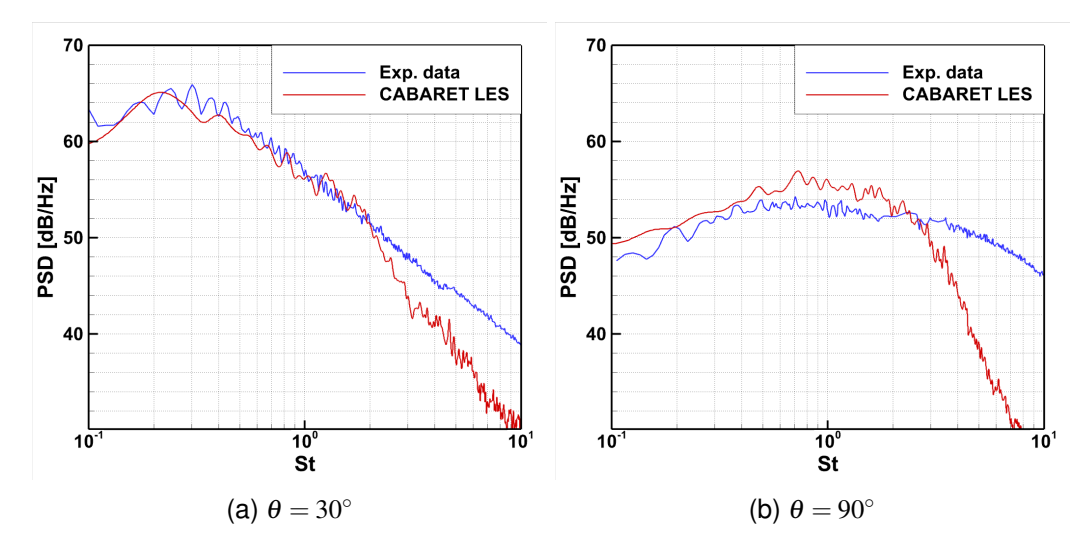


Figure 8 – Far-field sound PSD for SMC006 at $120D_i$ away from nozzle exit centre.

corresponds to approximately a Strouhal number ($St = fD_j/U_j$) of St = 2.0, which is determined by the mesh resolution as well as the time step size.

3.3 Design Variables

Two nozzle parameters, chevron penetration angle and chevron length, are selected as design variables in this study. As shown in Fig. 9a, one set of control points are placed on the centerline of the inner surface of the six chevrons. For SMC-type nozzles, the inner wall contracts along the axial direction and has a final 5° taper. The chevrons can be bent to increase or decrease the penetration, and the bent chevron has a slight curvature ($2\,cm$ radius of curvature) at its base. Figure 9b illustrates the perturbation of the control points by varying chevron penetration. Note that the baseline SMC006 geometry has a penetration angle of 18.2° , and the chevron length of the baseline model is denoted as L.

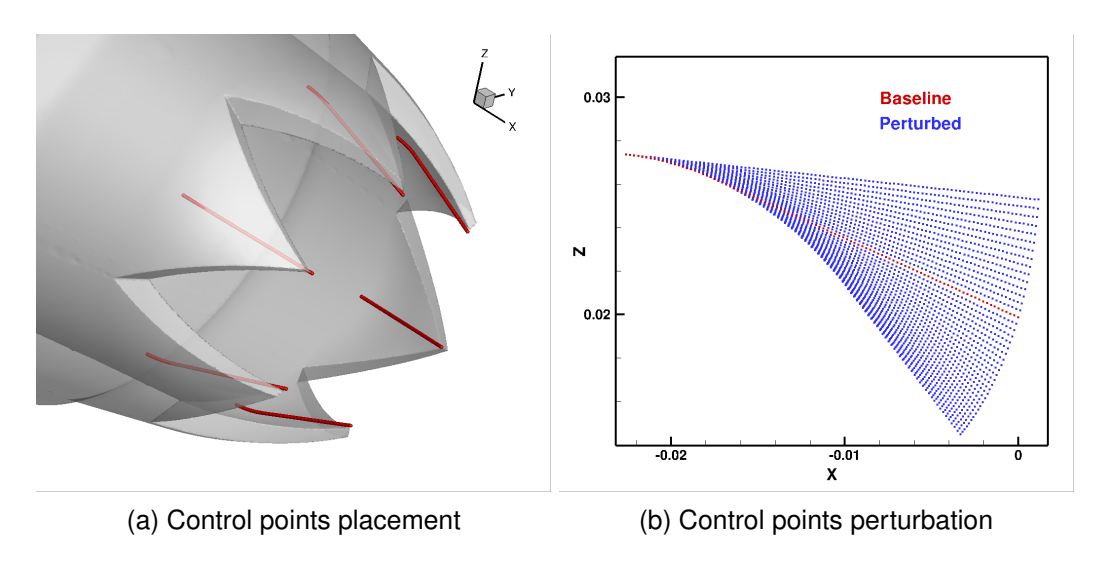
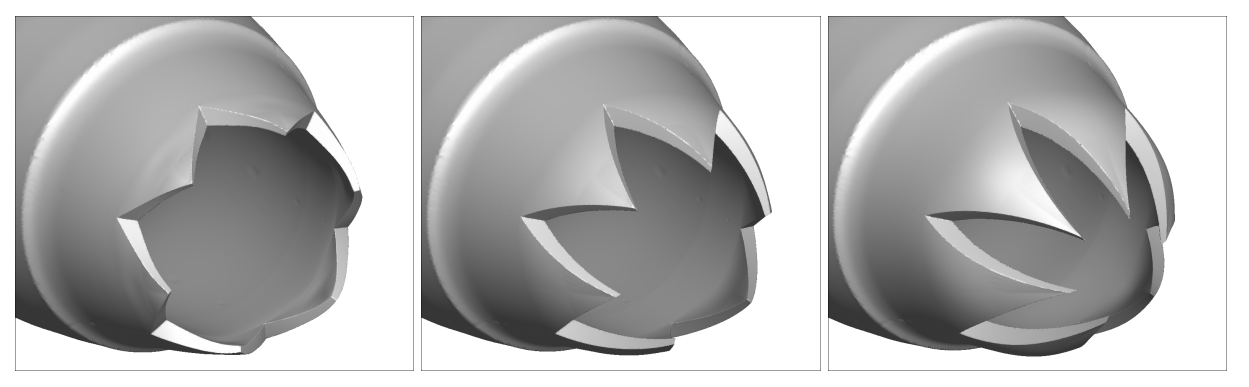


Figure 9 – Control points used for SMC006 surface control and mesh deformation.

Figure. 10 shows one set of deformed nozzle geometries by varying the penetration angle as well as chevron length via the RBF approach. The resulting nozzle geometries maintain a high level of smoothness, particularly for the chevrons, which is desirable for the flow-solver. As demonstrated in Fig. 11, the RBF mesh deformation method also enables an effective exploration of the design space through large surface perturbations.



(a) Penetration: 10°, Length: 0.5L (b) Penetration: 20°, Length: 1.0L (c) Penetration: 30°, Length: 1.5L

Figure 10 – Perturbed nozzle exit geometries for SMC006 with variation of penetration angle and chevron length.

3.4 Design Constraint

Thrust and mass flow rate are two of the key nozzle performance characteristics, and thrust is chosen as the design constraint for the optimisation case. The thrust penalty associated with the designs must be minimised wherever possible. The formulation used for calculating nozzle thrust is given as

$$T = \rho_e U_e^2 A_e + (P_e - P_a) A_e \tag{1}$$

where the subscript *e* represents nozzle exit, and *a* represents atmospheric properties.

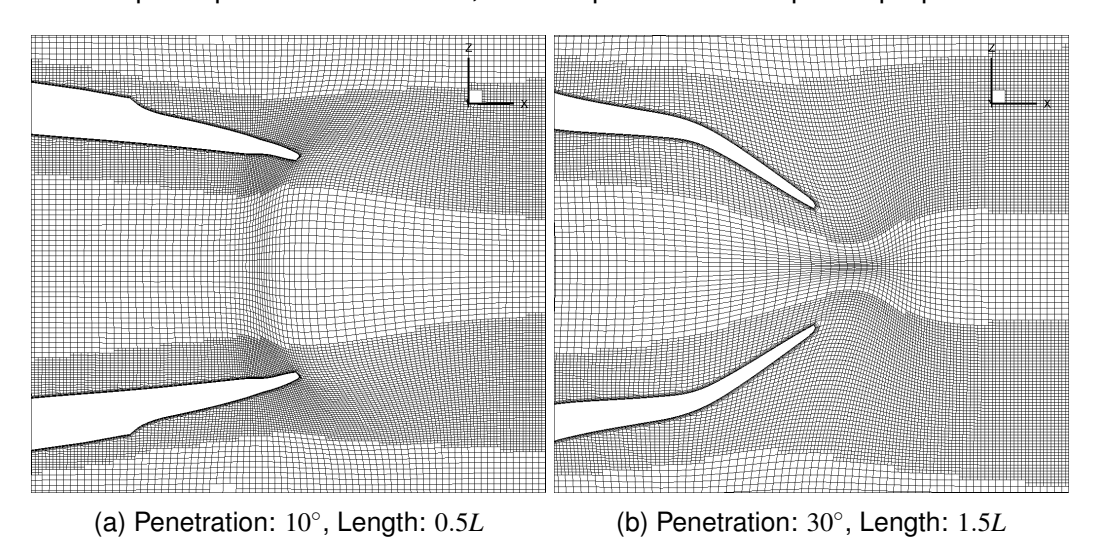


Figure 11 – Mesh deformation on the symmetry plane with perturbation of two design parameters.

The thrust calculation for chevron nozzles, however, remains a problem in the research community as determining the throat area of a chevron nozzle is difficult. In Reference [2], an effective nozzle diameter was determined by measuring the mass flow and was used as a surrogate area measurement. In current work, the thrust value is estimated by directly measuring the perpendicular force exerted by the jet on a cross-flow slice downstream of the nozzle exit. A velocity threshold is defined to determine whether a specific mesh cell on the slice is inside the jet area or not. A parametric study was conducted to determine the slice location and associated parameters to compute the thrust for each simulated nozzle. It was found that both the thrust value and jet area are robust at $x/D_j=0.1$ with a threshold of 10% of centerline streamwise velocity. As such, the combination of these two parameter settings are employed for thrust calculation throughout this work. The thrust and mass flow rate for the baseline SMC006 model are summarised in Table 1, and compared with the numerical simulation by Engblom *et al.* [23].

For demonstration, Figure 12 shows the contours of streamwise velocity component U_x on the slice

Table 1 – Nozzle performance for the baseline SMC006 model

-	Thrust (N)	Mass flow rate (kg/s)
Present	260.1	0.896
Engblom et al.	249.4	0.848

 $x/D_j=0.1$ for a set of deformed nozzle cases. With increased penetration angle and/or chevron length, the U_x contour becomes more star-shaped, reflecting the effect of chevrons on the flow-field.

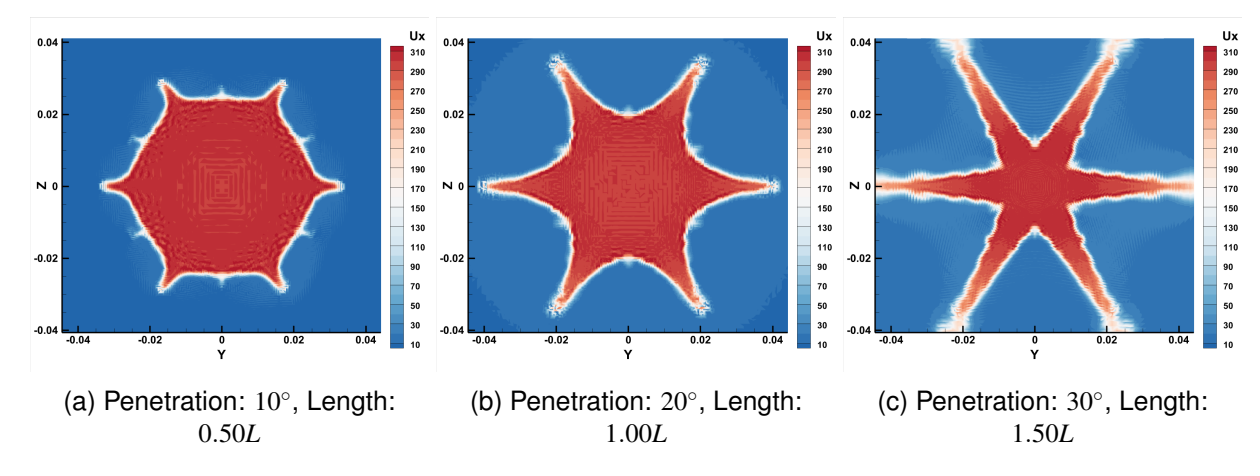


Figure 12 – Streamwise velocity contour on the slice $x/D_j=0.1$ for a set of deformed SMC006 nozzle cases.

3.5 Design Objective

The far-field noise signature is considered to be the design objective in the present work. As shown previously in Fig. 8, a good agreement is observed for the PSD data up to a cut-off frequency of St=2.0. Therefore, the band-limited overall sound pressure level (OASPL) is calculated and used as the objective function. The lower bound and upper bound of the band spectrum correspond to St=0.1 and St=2.0, respectively. Figure 13 shows the OASPL results at different polar angles for the baseline SMC006 geometry. Note that the FW-H integrals are calculated at $120D_j$ away from nozzle exit centre.

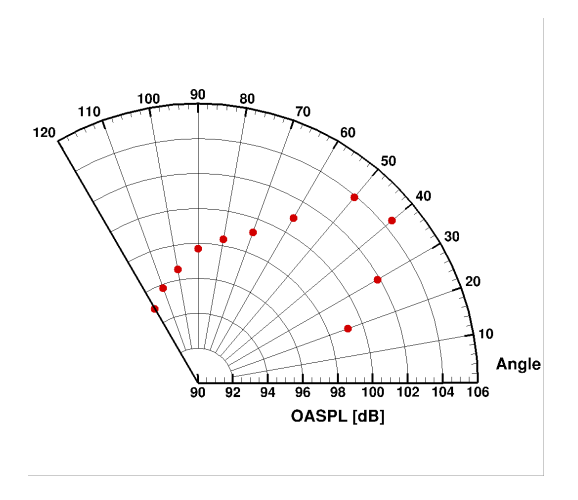


Figure 13 – Far-field band-limited OASPL for the baseline SMC006 nozzle at $R = 120D_i$.

4. Initial Results and Discussion

This section presents the initial results for the surrogate model built for the SMC006 aeroacoustic optimisation. A number of sampling points were distributed in the design space, and CABARET LES

was performed at these points. Surrogate models were built for both constraint and objective functions. A further thrust correction step was implemented to meet the design constraint requirement, and associated simulations were performed for the perturbed geometries.

4.1 Surrogate Modelling for Thrust

The surrogate was built using two evenly-distributed sets of sampling points, distributed in the two-dimensional design space. A set of 49 cases (i.e. 7×7 matrix of design points) covers the boundaries of the design space, where the lower and upper bounds for penetration angle are 5° and 35° , and chevron length ranges from 0.5L to 1.5L. A further set of 36 cases (i.e. 6×6 matrix of design points) were then placed in the cell centres formed by the first set. Hence, a total number of 85 sampling points are used to build the surrogate models for the quantities of interest.

The results obtained from the LES simulations were used to build the surrogate model using an RBF interpolation. Figure 14a shows the response surface of the jet thrust. It is worthing noting that the thrust surface is very smooth, but the thrust variation is large, ranging approximately from 175N to 315N. This indicates that the aerodynamic performance of the jet nozzle is very sensitive to the perturbation of the two design parameters.

Thrust is a key index for measuring jet nozzle performance, and the jet thrust of baseline SMC006 can be treated as an equality constraint in the optimisation. Thrust correction is performed by further perturbing the nozzle exit area for the deformed nozzle geometry to compute the thrust gradient, which is then used to compute an effective area change required to balance the thrust.

A surrogate model was thus built for obtaining the results of local thrust gradient dT/dA at any location in the design space. For the set of 49 sampling points, a constant delta radius of 0.25mm (i.e. equivalent to approximately 0.5% of D_j) was added to the nozzle exit radius (i.e. inner radius of chevron tip), the mesh deformed and an extra batch of 49 LES runs performed to calculate the delta thrust and hence the thrust gradient dT/dA. These runs were very cheap due to only being run for sufficient time units to obtain the thrust value, rather than acoustic data.

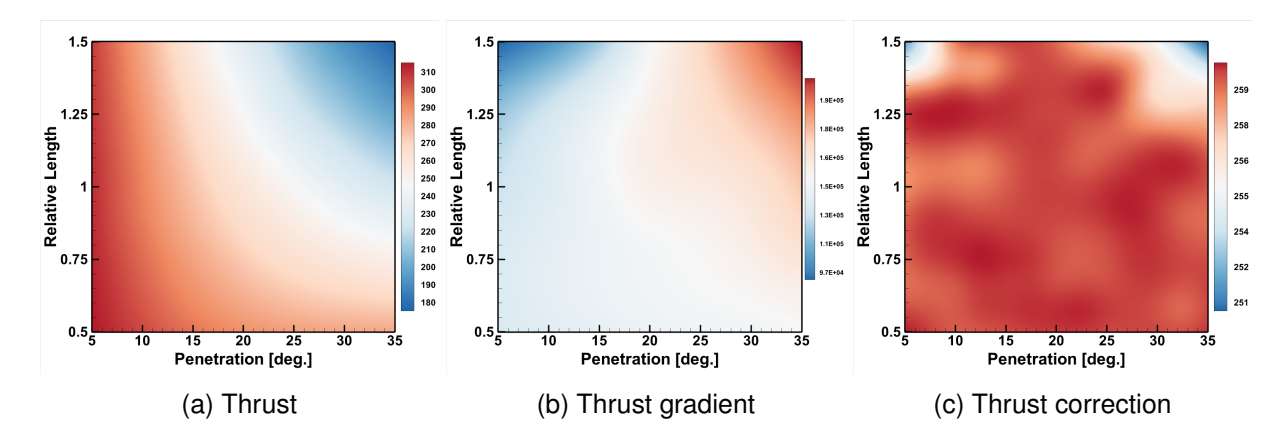


Figure 14 – Thrust response surfaces for the SMC006 surrogate model.

The surrogate model of thrust gradient is illustrated in Fig. 14b. Area perturbations were then implemented for all the 85 sampling cases, based on the thrust gradient information, and all cases rerun. The resulting thrust values are shown in Fig. 14c. There is some minor variation from the baseline value, but this is within the thrust tolerance for SMC006 optimisation. Figure 15 shows two representative cases with area perturbation of the nozzle exit, i.e. the nozzle and mesh have already been deformed via the chevron parameters, shown as the blue surfaces, and are then further deformed to correct the thrust value. Note that the support radius is set with a larger value, for example $4.0D_j$ is used here, to ensure the exit area perturbation can be propagated gradually upstream towards the nozzle inlet.

4.2 Surrogate Modelling for Noise Signature

Figures 16 shows the response surfaces of band-limited OASPL at several observer polar angles. Interestingly, the surrogate models point towards different directions for the optimum if the design

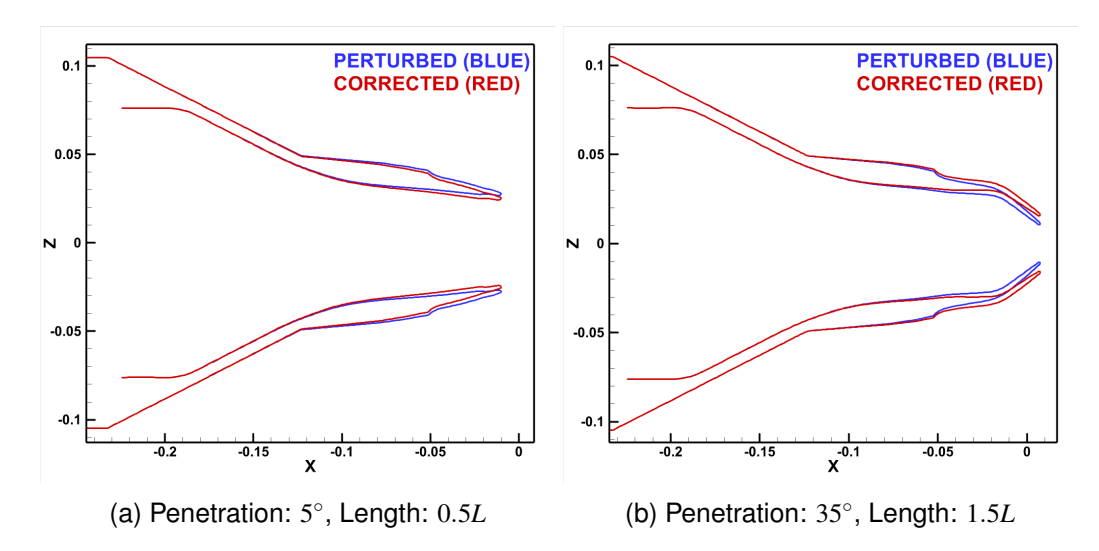


Figure 15 – Area perturbation of the SMC006 nozzle exit for thrust correction.

objective is defined as the OASPL at individual observer angles. There is a strong reduction of OASPL at low observation angles by increasing both the chevron length and penetration, with this dependence reversing at higher observer angles. To further investigate this phenomenon, the band-limited OASPL is plotted in Fig. 17 for all 11 observer angles with one design parameter perturbed for the baseline geometry. When the penetration or chevron length is enlarged, the OASPL decreases at 20° and 30° but increases at other polar angles. There exists a turning point between 30° and 40° . The pattern observed from OASPL variations explains the fact that different optimum locations are found when setting objective function to individual observation angles. This is very similar to the scenario of single-point optimisation, where a specific optimised result is obtained but does not hold up robustly for all locations.

As such, a compound OASPL objective function is considered by taking a combination of multiple observer angles. Figure 18 shows the results of OASPL response surfaces with different combinations of polar angles used as compound objective function. Compared with the results presented in Fig. 16, the response surfaces are significantly more flat for a compound objective function. It is worth noting that all surrogate models suggest an optimum locating at a corner point of the response surface, which may indicate that the design space needs to be enlarged in order to encapsulate the global optimum. Nonetheless, considering the acoustic pattern demonstrated in Fig. 17, it is not surprising that optimum points are observed at the boundaries of the design space. The surrogate modelling results reflect the necessity to propose alternative objective functions for jet aeroacoustic optimisation, for example, minimisation of the peak PSD or SPL within a limited frequency range.

4.3 Multi-objective Optimisation

The thrust of the chevron nozzle was previously treated as the design constraint. Alternatively, it can be considered as a design objective in aeroacoustic optimisation where the thrust for the desired design shall be no smaller than its original value. As such, a surrogate model was built without performing thrust correction step. Figure 19 shows the results of the sampling points with respect to the two design objectives at two representative observer locations. The x axis shows the percentage of thrust loss, with a positive value representing a decrease of thrust compared with the baseline geometry, and a negative value meaning an increase in thrust. The y axis shows the variation of OASPL at a specific polar angle, with a positive value representing an increase of noise signature and a negative value meaning a noise reduction. Following this definition, the baseline case is located at the origin point (0,0), and is labelled as red in the graphs. If a sample point falls into the third quadrant, i.e. lower-left sector of the coordinate plane, it can achieve noise reduction as well as thrust increase simultaneously, and hence would be a desirable design case.

As shown in Fig. 19a, the results for 30° polar angle demonstrates a clear trend that the points are clustering in the fashion of linear distribution. Among all sampling points, the cases located in the

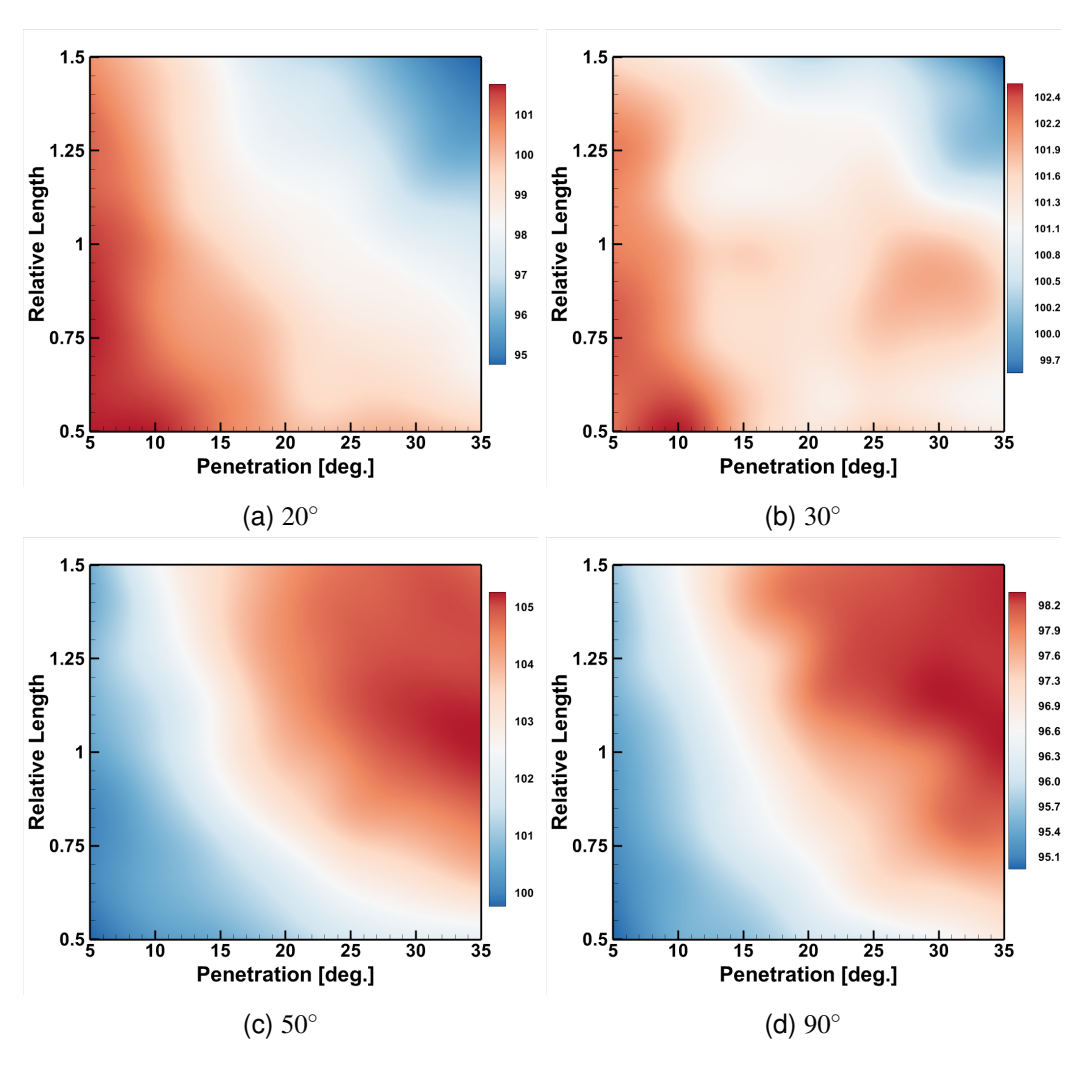


Figure 16 – Response surfaces (with thrust correction) of the objective function with OASPL collected at individual observer polar angles.

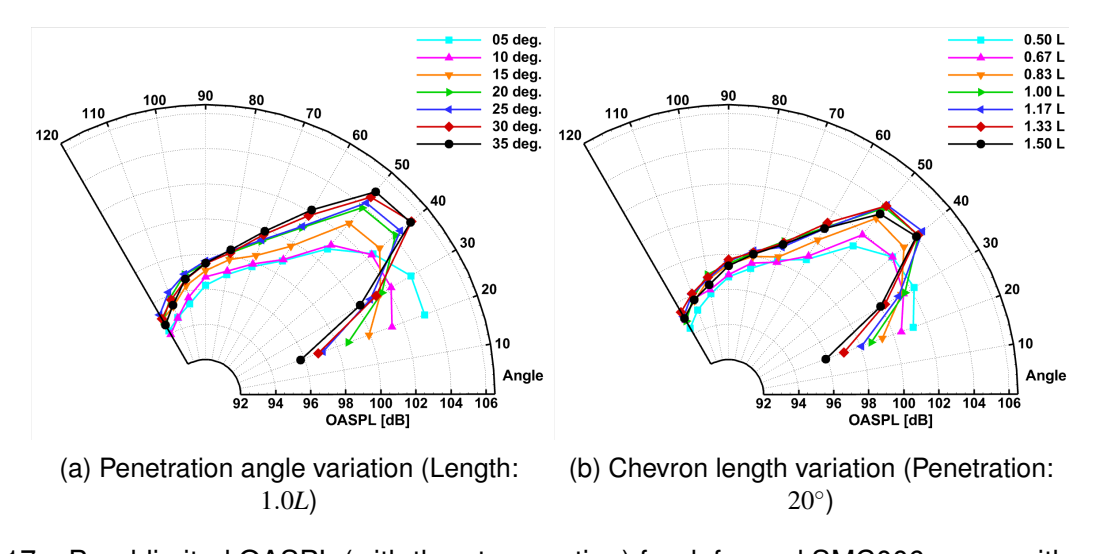


Figure 17 – Band-limited OASPL (with thrust correction) for deformed SMC006 cases with variation of one design parameter.

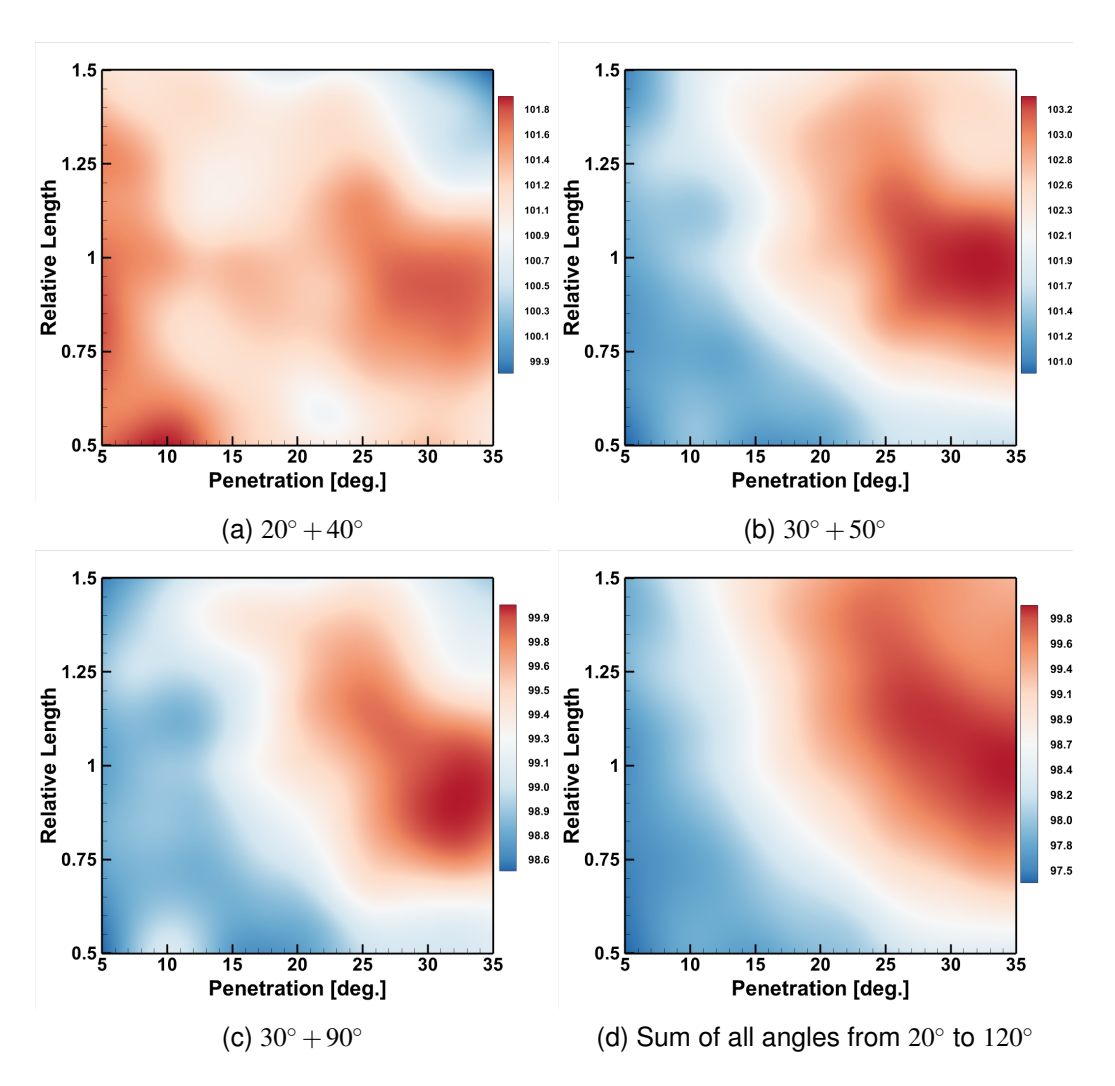


Figure 18 – Response surfaces (with thrust correction) of the compound objective function with OASPL collected from combinations of multiple observer polar angles.

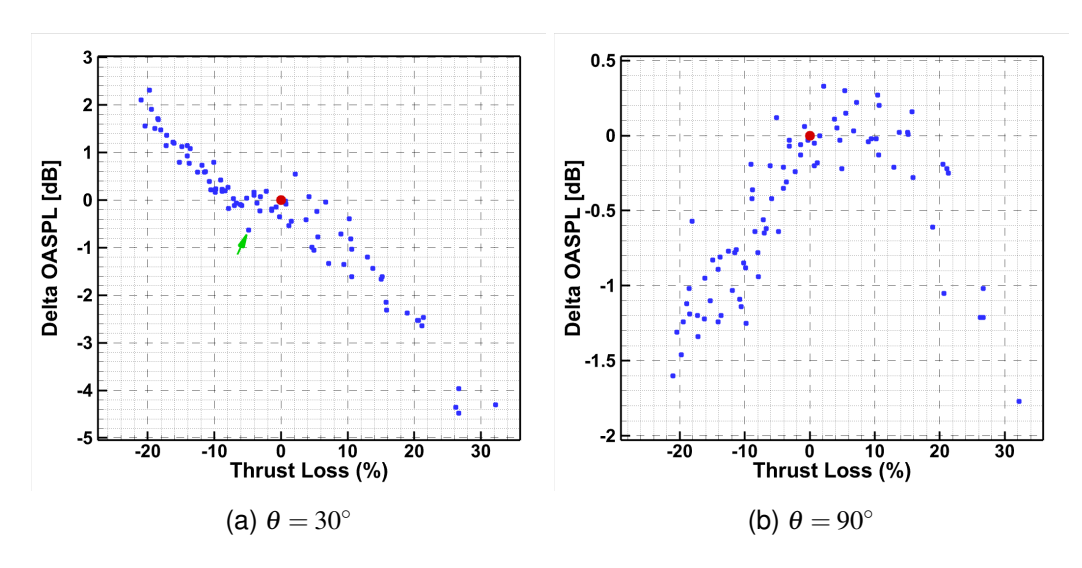


Figure 19 – Multi-objective optimisation results at two representative observer polar angles.

bottom-right corner have the largest amount of noise reduction but also come with the largest thrust loss, as they feature the maximum in both penetration angle and chevron length. Nonetheless, it is worth observing that there are some points falling onto the third quadrant of the plot. For instance, the design case shown by the green arrow is on the Pareto front and has a smaller chevron angle (12.5°) and a larger chevron length (1.417L) compared with the baseline geometry. Although the level of noise reduction is not significant, it still indicates that we could improve both the aerodynamic and acoustic performance at this observation polar angle, and further improvement could be achieved if more sampling points are placed in this region of the design space.

When the OASPL at 90° polar angle is chosen as the noise objective, the corresponding results are shown in Fig. 19b. The cloud of sampling points has a shape of an arc, and the points at the two corners of the arc correspond to nozzle cases with large shape perturbations. It is apparent that the points located in the bottom-right quadrant are not favourable as they face a thrust loss penalty; whereas the group of points in the bottom-left quadrant fulfil both design objectives. However, it should be noted that the optimal design case has the smallest penetration angle (5°) and chevron length (0.5L), i.e. lower bound of the two design variables, indicating that further improvement could be achieved if the design space is enlarged.

5. Conclusions

A surrogate model-based optimisation framework has been developed to allow acoustic optimisation of jet nozzle exit geometries. The optimisation framework is wrapped around an efficient LES solver, which is based on the CABARET scheme and is implemented on GPUs to ensure the run-time is practical. The CABARET LES solutions are further coupled with the FW–H method for far-field noise predictions. The design space is modelled with nozzle chevron parameterisation, with the initial results presented here using chevron length and penetration as the design parameters. Effective geometric shape control and volume mesh deformation is achieved via an RBF volume interpolation approach with an efficient data reduction algorithm. Surrogate models are built for both thrust constraint as well as noise objective functions based on the OASPL values. Initial cases have been run using a design-space modelling and investigation approach, rather than strict optimisation.

The effectiveness, efficiency and robustness of the method has been demonstrated, and initial results shown for cases with a thrust constraint. The significance of the thrust constraint and the objective function definition on the results have been shown via both single and multi-objective optimisations. There is a strong reduction of OASPL at low observation angles by increasing both the chevron length and penetration, with this dependence reversing at higher observer angles. There is a more limited impact on overall OASPL, i.e. the sum over all observer angles, with lower chevron length and penetration appearing favourable with the thrust constraint.

Future work will include adaptive surrogate model-based optimisation for both isolated and installed jet configurations. A mixed continuous-discrete design space will also be modelled, with more design parameters being considered, such as chevron count, nozzle scarfing and eccentricity.

6. Acknowledgements

The first author would like to acknowledge the financial support from the Laboratory of Aerodynamic Noise Control (Grant No. ANCL20230305) and also from the National Key Laboratory of Aircraft Configuration Design (Grant No. 61422010301). Part of the simulations were carried out using the computational facilities of the Advanced Computing Research Centre, University of Bristol. (https://www.bristol.ac.uk/acrc)

7. Contact Author Email Address

guangda.yang@bristol.ac.uk

8. Copyright Statement

The authors confirm that they, and/or their company or organization, hold copyright on all of the original material included in this paper. The authors also confirm that they have obtained permission, from the copyright holder of any third party material included in this paper, to publish it as part of their paper. The authors confirm that

they give permission, or have obtained permission from the copyright holder of this paper, for the publication and distribution of this paper as part of the ICAS proceedings or as individual off-prints from the proceedings.

References

- [1] Papamoschou D and Debiasi M. Directional suppression of noise from a high-speed jet. *AIAA Journal*, 39(3):380–387, 2001.
- [2] Bridges J and Brown C. Parametric testing of chevrons on single flow hot jets. In *10th AIAA/CEAS Aeroacoustics Conference*, page 2824, 2004.
- [3] Papamoschou D. New method for jet noise reduction in turbofan engines. *AIAA Journal*, 42(11):2245–2253, 2004.
- [4] Viswanathan K, Shur M, Strelets M, and Spalart P. Numerical prediction of noise from round and beveled nozzles. In *Turbulent Flow and Noise Generation, EUROMECH Colloquium 467, Marseille, France*, 2005.
- [5] Fabiano E, Mishra A, Yang Z, and Mavriplis D. Towards adjoint-based sensitivity analysis for supersonic jet noise. In *AIAA Aviation 2020 Forum*, page 3131, 2020.
- [6] Ruscher C, Gogineni S, and Papamoschou D. Novel methodology for the rapid acoustic optimization of supersonic multi-stream 3D nozzles. In *NASA Acoustics Technical Working Group Presentation*, 2021.
- [7] Karabasov S and Goloviznin V. New efficient high-resolution method for nonlinear problems in aeroacoustics. *AIAA Journal*, 45(12):2861–2871, 2007.
- [8] Karabasov S and Goloviznin V. Compact accurately boundary-adjusting high-resolution technique for fluid dynamics. *Journal of Computational Physics*, 228(19):7426–7451, 2009.
- [9] Faranosov G, Goloviznin V, Karabasov S, Kondakov V, Kopiev V, and Zaitsev M. CABARET method on unstructured hexahedral grids for jet noise computation. *Computers & Fluids*, 88:165–179, 2013.
- [10] Markesteijn A and Karabasov S. GPU CABARET solutions for the nasa shjar jet noise experiment: Flow and noise modeling. In *23rd AIAA/CEAS Aeroacoustics Conference*, page 3852, 2017.
- [11] Markesteijn A and Karabasov S. CABARET solutions on graphics processing units for NASA jets: grid sensitivity and unsteady inflow condition effect. *Comptes Rendus Mécanique*, 346(10):948–963, 2018.
- [12] Markesteijn A, Gryazev V, Karabasov S, Ayupov R, Benderskiy L, and Lyubimov D. Flow and noise predictions of coaxial jets. *AIAA Journal*, 58(12):5280–5293, 2020.
- [13] Mukha T, Rezaeiravesh S, and Liefvendahl M. A library for wall-modelled large-eddy simulation based on openfoam technology. *Computer Physics Communications*, 239:204–224, 2019.
- [14] Saad T, Cline D, Stoll R, and Sutherland J. Scalable tools for generating synthetic isotropic turbulence with arbitrary spectra. *AIAA Journal*, 55(1):327–331, 2017.
- [15] Semiletov V and Karabasov S. Cabaret scheme with conservation-flux asynchronous time-stepping for nonlinear aeroacoustics problems. *Journal of Computational Physics*, 253:157–165, 2013.
- [16] Rendall T and Allen C. Unified fluid–structure interpolation and mesh motion using radial basis functions. *International Journal for Numerical Methods in Engineering*, 74(10):1519–1559, 2008.
- [17] Poole D, Allen C, and Rendall T. High-fidelity aerodynamic shape optimization using efficient orthogonal modal design variables with a constrained global optimizer. *Computers & Fluids*, 143:1–15, 2017.
- [18] Mackman T and Allen C. Investigation of an adaptive sampling method for data interpolation using radial basis functions. *International Journal for Numerical Methods in Engineering*, 83:915–938, 2010.
- [19] Rendall T and Allen C. Reduced surface point selection options for efficient mesh deformation using radial basis functions. *Journal of Computational Physics*, 229(8):2810–2820, 2010.
- [20] Sheng C and Allen C. Efficient mesh deformation using radial basis functions on unstructured meshes. *AIAA Journal*, 51(3):707–720, 2013.
- [21] Kedward L, Allen C, and Rendall T. Efficient and exact mesh deformation using multiscale RBF interpolation. *Journal of Computational Physics*, 345:732–751, 2017.
- [22] Wendland H. Piecewise polynomial, positive definite and compactly supported radial functions of minimal degree. *Advances in Computational Mathematics*, 4(1):389–396, 1995.
- [23] Engblom W, Khavaran A, and Bridges J. Numerical prediction of chevron nozzle noise reduction using wind-mgbk methodology. In 10th AIAA/CEAS Aeroacoustics Conference, page 2979, 2004.
- [24] Tanna H. An experimental study of jet noise Part I: Turbulent mixing noise. *Journal of Sound and Vibration*, 50(3):405–428, 1977.
- [25] Angelino M, Xia H, Moratilla-Vega M, and Page G. Far-field noise prediction of round and serrated jets with increasingly refined grids. In *22nd AIAA/CEAS Aeroacoustics Conference*, page 3047, 2016.
- [26] Brown C and Bridges J. Small hot jet acoustic rig validation. NASA TM, 214234:2006, 2006.